

Constraints on Deep-seated Zonal Winds Inside Jupiter and Saturn

Junjun Liu

100-23, Geological and Planetary Sciences, Caltech, Pasadena, CA 91125.

E-mail: ljj@gps.caltech.edu

Peter M. Goldreich

School of Natural Sciences, Institute for Advanced Study, Princeton, NJ 08540.

E-mail: pmg@ias.edu

David J. Stevenson

150-21, Geological and Planetary Sciences, Caltech, Pasadena, CA 91125.

E-mail: djs@gps.caltech.edu

Submitted to Icarus.

Manuscript pages including references and figure captions: 24. Number of figures: 12.

Keywords: (1) MAGNETIC FIELDS, (2) ATMOSPHERES, DYNAMICS, (3) INTERIORS.

Proposed running head:

Constraints on Deep-seated Zonal Winds Inside Jupiter and Saturn

Send proofs and correspondence to:

Junjun Liu

100-23, Geological and Planetary Sciences,

Caltech,

Pasadena, CA 91125.

E-mail: lijj@gps.caltech.edu

Phone: (626)-395-6894

Fax: (626)-585-1917

Abstract

The atmospheres of Jupiter and Saturn exhibit strong and stable zonal winds. How deep the winds penetrate unabated into each planet is unknown. Our investigation favors shallow winds. It consists of two parts.

The first part makes use of an Ohmic constraint; Ohmic dissipation associated with the planet's magnetic field cannot exceed the planet's net luminosity. Application to Jupiter (J) and Saturn (S) shows that the observed zonal winds cannot penetrate below a depth at which the electrical conductivity is about six orders of magnitude smaller than its value at the molecular-metallic transition. Measured values of the electrical conductivity of molecular hydrogen yield radii of maximum penetration of $0.96R_J$ and $0.86R_S$, with uncertainties of a few percent of R . At these radii, the magnetic Reynolds number based on the zonal wind velocity and the scale height of the magnetic diffusivity is of order unity. These limits are insensitive to difficulties in modeling turbulent convection. They permit complete penetration along cylinders of the equatorial jets observed in the atmospheres of Jupiter and Saturn.

The second part investigates how deep the observed zonal winds actually do penetrate. As it applies heuristic models of turbulent convection, its conclusions must be regarded as tentative. Truncation of the winds in the planet's convective envelope would involve breaking the Taylor-Proudman constraint on cylindrical flow. This would require a suitable nonpotential acceleration which none of the obvious candidates appears able to provide. Accelerations arising from entropy gradients, magnetic stresses, and Reynolds stresses appear to be much too weak. These considerations suggest that strong zonal winds are confined to shallow, stably stratified layers, with equatorial jets being the possible exception.

1. Introduction

Jupiter and Saturn, are composed primarily of hydrogen and helium with small additions of heavier elements. Their atmospheres exhibit strong, stable zonal winds composed of multiple jets associated with azimuthal cloud bands (Ingersoll 1990). Zonal winds peak in the equatorial region reaching $\sim 100 \text{ m s}^{-1}$ on Jupiter and $\sim 400 \text{ m s}^{-1}$ on Saturn.¹ The latitudes of Jupiter's jets have not changed for at least 80 years (Smith & Hunt 1976) and their velocities have been constant within 10% over 25 years (Porco et al. 2003).

The depth of the zonal winds is unknown. Both deep and shallow flow models have been proposed. Wind speeds measured by the Galileo probe at $7.4^\circ N$ on Jupiter rose from 90 m s^{-1} at 0.4 bar to 180 m s^{-1} at ~ 5 bar and then remained nearly constant until 22 bar (Atkinson et al. 1997, 1998). It is important to bear in mind that these measurements only sample the winds in the outer 1% of the planet's radius where the electrical conductivity is low. In regions of high electrical conductivity, the magnetic field lines are frozen into the fluid. Winds in these regions would cause changes in the external magnetic field. By comparing Galileo and Pioneer/Voyager data, Russell et al. (2001a,b) find that increases of 0.3 deg in the dipole tilt and 1.5% in Jupiter's dipole moment may have taken place between 1975 and 2000. The former could be accounted for by meridional flows with speeds in the deep interior of order 0.1 cm s^{-1} (Guillot et al. 2004).

Busse (1976, 1983, 1994) advocates deep flows. He applies the Taylor-Proudman theorem (Taylor 1923) to deduce that zonal flows extend along cylinders oriented parallel the rotation axis in the molecular envelope, and then terminate at the outer boundary of the metallic core where he assumes that hydrogen undergoes a first order phase transition. But data from shock wave experiments show that hydrogen undergoes a continuous transition from a semi-conducting

¹Wind speeds on Jupiter are determined relative to System III coordinates which rotate with the angular speed of the planet's magnetic field (Dessler 1983). Only differences among wind speeds on Saturn are known because the planet's internal rotation rate is uncertain.

molecular state to a highly conducting metallic state as the pressure increases. This contradicts the assumption of a first order phase transition at the core-envelope boundary.

Recently, a modified deep flow model for Jovian zonal flows has been proposed based on simulations of convection in a shell with a lower boundary near $0.9R_J$ (Aurnou & Heimpel 2004; Heimpel et al. 2005). The physical meaning of the lower boundary in the modified deep flow model is obscure. Hydrogen cannot undergo a phase change at that radius (Guillot et al. 2004). So how might the Taylor-Proudman constraint be violated in order to reduce the zonal flow to a near zero value below that boundary? We address related issues in §5.

In shallow flow models, the observed high-speed flow is confined to a thin, baroclinic layer near the cloud level; the interior flow is much slower. Even if the high velocity flow is confined to a shallow layer, its forcing may occur at depth. For example, if the flow were to arise from a process that conserved angular momentum per unit volume, ρU would be approximately conserved, where ρ is the density and U is the magnitude of the flow velocity. Since the density in the interior is several orders of magnitudes larger than that near the surface, the flow velocity could then be much greater near the surface. On the other hand, the observed zonal flow might be generated by shallow forcing due to the turbulence injected at the cloud level by moist convection, differential latitudinal solar heating, latent heat release from condensation of water, or other weather layer processes (Vasavada & Showman 2005). From the thermal wind equation, a latitudinal temperature gradient of about $5 - 10K$ across a few pressure scale heights below the cloud level would cause substantial vertical shear, which makes the flow velocity much greater near the surface than deeper down (Ingersoll & Cuzzi 1969; Ingersoll et al. 1984; Vasavada & Showman 2005).

The plan of our paper is as follows. Relevant details of the electrical conductivity of molecular hydrogen as measured in shock wave experiments are presented in §2. Sections 3 and 4 are devoted to the calculation of Ohmic dissipation based on the assumption that the zonal wind

penetrates the planet along cylinders. In the former, the poloidal magnetic field is determined by downward extrapolation of the external field. This procedure is appropriate in regions where the magnetic Reynolds based on the convective velocity, $R_m^c \ll 1$. In the latter, we examine the consequences of assuming that the poloidal magnetic field is parallel to the rotation axis in regions where $R_m^c \gg 1$. The requirement that the total Ohmic dissipation be bounded from above by the planet's net luminosity, \mathcal{L} , limits the depth to which the observed zonal winds can penetrate. Section 5 asks whether the zonal winds might be truncated within the convective envelope. A short summary of our main results is given in §6. A few technical details are relegated to the Appendix.

2. Electrical Conductivity In Jupiter & Saturn

Electrical conductivity in the interiors of Jupiter and Saturn is due mainly to hydrogen. Near their surfaces it might be significantly enhanced relative to pure hydrogen by the addition of some more readily ionized heavier elements. Helium is unimportant due to its high ionization potential.

Condensed molecular hydrogen is a wide band-gap insulator at room temperature and pressure, with a band gap, E_g , of about 15 eV, corresponding to the ionization energy of the hydrogen molecule. As the pressure increases, this gap is expected to diminish and finally close to zero, resulting in an insulator-to-metal transition. In experiments, this transition appears to be gradual. As the energy gap closes, hydrogen molecules begin to dissociate to monatomic hydrogen and electrons start to be delocalized from H_2^+ ions (Nellis et al. 1996; Weir et al. 1996). The insulator-to-metal transition is expected to occur even though the hydrogen molecules have not been fully pressure-dissociated. At much higher pressure and temperature, molecular dissociation becomes complete and it is presumed that pure monatomic hydrogen forms a metallic Coulomb plasma (Stevenson & Ashcroft 1974; Hubbard et al. 1997).

The conductivity of hydrogen has been measured in reverberating shock wave experiments from 0.93 Mbar to 1.8 Mbar (Weir et al. 1996; Nellis et al. 1999) and in single shock experiments from 0.1 Mbar to 0.2 Mbar (Nellis et al. 1992). In these experiments, hydrogen is in thermal equilibrium at pressures and temperatures similar to those in the interiors of giant planets. From 0.93 to 1.4 Mbar, the measured electrical conductivity of hydrogen increases by four orders of magnitude. Between 1.4 Mbar and 1.8 Mbar, the conductivity is constant at $2 \times 10^5 \text{ S m}^{-1}$, similar to that of liquid Cs and Rb at 2000 K and two orders of magnitude lower than that of a good metal (e.g. Cu) at room temperature. The constant conductivity suggests that the energy gap has been thermally smeared out (Weir et al. 1996). Temperatures of shock-compressed liquid hydrogen have been measured optically in separate experiments (Nellis et al. 1995; Holmes et al. 1995). At the highest obtained pressure of 0.83 Mbar, the measured temperature of 5200 K falls below that predicted for pure molecular hydrogen. This is due to the dissociation of molecular hydrogen and enables us to estimate the fractional dissociation as a function of pressure. At 1.4 Mbar and 3000 K, the dissociation fraction is $\sim 5\%$. Thus metallization of hydrogen occurs in the diatomic molecular phase and is caused by electrons delocalized from H_2^+ ions (Nellis et al. 1996; Ashcroft 1968). Since we are interested in the outer shell of the giant planets, the measurements at 0.1 – 0.2 Mbar are the most relevant. In this low-pressure range, the dissociation of hydrogen molecules is unimportant.

The electrical conductivity of a semiconductor can be expressed in the form:

$$\sigma = \sigma_0(\rho) \exp\left(-\frac{E_g(\rho)}{2K_B T}\right), \quad (1)$$

where σ is electrical conductivity, $E_g(\rho)$ is the energy of the density dependent mobility gap, K_B is Boltzmann's constant, T is the temperature, and $\exp(-E_g/2K_B T)$ expresses the fractional occupancy of the current carrying states. The conductivity measurement at 0.27 g cm^{-3} and a temperature of 4160 K ² (Nellis et al. 1992) is close to the interior isentropes of Jupiter and Saturn (Guillot 1999). This measurement determines $\sigma_0 = 1.1 \times 10^8 \text{ S m}^{-1}$ and $E_g = 11.7 \pm 1.1 \text{ eV}$. The

²The corresponding pressure is 0.187 Mbar.

error bar in the energy gap comes from the experimental uncertainties in σ and uncertainties in calculated post-shock temperatures (Nellis et al. 1995).

The data suggest that it is sufficiently accurate to assume E_g is a linear function of hydrogen density ρ_{H_2} : $E_g = a + b\rho_{H_2}$, where a and b are two constants (Nellis et al. 1992, 1996). The measurements and the energy gap (15eV) at room temperature and pressure determine the values of a and b . Since the volume mixing ratio of hydrogen in the outer shells of giant planets is about 92%, the density in giant planet interiors is $1.18\rho_{H_2}$. With σ_0 , $E_g(\rho_{H_2})$, and $T(\rho)$ from the planetary interior model (Guillot 1999), the conductivity profiles of the giant planets can be calculated.

Figure (1) displays the conductivity distributions as a function of radius in the outer shells of Jupiter and Saturn. The conductivity increases with depth, and there is a smooth transition from semi-conducting to metallic hydrogen at pressure (1.4 Mbar). This transition takes place at about 0.84 of Jupiter's radius and 0.63 of Saturn's radius.

The electrical conductivity is proportional to the total number density of electrical charge carriers: $\sigma \propto n_e$, which includes a contribution, which we have neglected, from impurities x in addition to that from hydrogen:

$$n_e = n_{H_2} \exp\left(-\frac{E_g}{2K_B T}\right) + \sum_x n_x \exp\left(-\frac{E_x}{2K_B T}\right), \quad (2)$$

where n_x and E_x express the number density of the electrons and the energy gap due to an impurity. Alkali metals are sources of small band gap impurities. They may also contribute to the radiative opacity thus insuring adiabaticity (Guillot et al. 2004; Guillot 2005). The mixing ratio of an alkali metal in the interior of a giant planet is presumably similar to that determined from its cosmic abundance. With these abundances, a band gap of a few electron volts would lead to a conductivity of $10^{-6} \sim 10^{-4} \text{ S m}^{-1}$ at $T \sim 1000 \text{ K}$, significantly above the value due to hydrogen in the outer shells of giant planets.

In magnetohydrodynamics it is conventional to characterize the electrical conductivity σ in terms of the magnetic diffusivity $\lambda = (\mu_0\sigma)^{-1}$, where μ_0 is the magnetic permeability. Figure (1) shows that the electrical conductivity of hydrogen decreases exponentially outward from the metallic conducting region. Therefore, the magnetic diffusivity increases exponentially outward. The scale height of magnetic diffusivity

$$H_\lambda(r) = \frac{\lambda(r)}{d\lambda(r)/dr} \quad (3)$$

is shown in figure (2).

3. Ohmic Dissipation Based On Inward Extrapolation Of The External Magnetic Field

We approximate the planet's magnetic field as axisymmetric; Jupiter's dipole tilt is about 10° and Saturn's less than 0.1° (Connerney 1993). Then we evaluate the azimuthal component of the magnetic field produced by differential rotation acting on the poloidal components. The maximum penetration depth is that of the level above which the associated Ohmic dissipation matches the planet's net luminosity, \mathcal{L} .

To proceed, we need to know the poloidal magnetic field above the maximum penetration depth. Here we assume that it can be determined by inward extrapolation of the planet's external magnetic field. This assumption is appropriate provided the magnetic Reynolds number based on the convective velocity field, R_m^c , remains small down to the maximum penetration depth, which our estimates suggest it does.³

Lack of accurate magnetic field measurements at high latitudes close to Jupiter and Saturn makes the inward extrapolation of their external magnetic fields somewhat uncertain. Thus we cannot exclude the possibility that where $R_m^c \gg 1$ the magnetic field might be closely aligned with the rotation axis. This possibility is examined in §4.

³An axisymmetric poloidal field is invariant under differential rotation.

a. Derivation of Ohmic dissipation

The time evolution of the magnetic field satisfies

$$\frac{\partial \mathbf{B}}{\partial t} = \nabla \times (\mathbf{U} \times \mathbf{B}) - \nabla \times [\lambda(r) \nabla \times \mathbf{B}] , \quad (4)$$

where \mathbf{U} and \mathbf{B} denote velocity and magnetic field. We work in spherical coordinates and set $\mathbf{U} = U_\phi \mathbf{e}_\phi = r \sin \theta \Omega \mathbf{e}_\phi$. The generation of toroidal field from poloidal field is described by

$$\begin{aligned} \frac{\partial B_\phi}{\partial t} = & r \sin \theta \left(\frac{\partial \Omega}{\partial r} B_r + \frac{1}{r} \frac{\partial \Omega}{\partial \theta} B_\theta \right) \\ & + \frac{1}{r} \frac{\partial}{\partial r} \left(\lambda \frac{\partial}{\partial r} (r B_\phi) \right) \\ & + \frac{\lambda}{r^2} \frac{\partial}{\partial \theta} \left(\frac{1}{\sin \theta} \frac{\partial}{\partial \theta} (\sin \theta B_\phi) \right) . \end{aligned} \quad (5)$$

We seek a steady state solution noting that B_ϕ scales proportional to λ^{-1} , and H_λ is much smaller than the length scale for the meridional variation of U_ϕ and B . Thus we neglect $r^{-1} \partial / \partial \theta$ with respect to $\partial / \partial r$, which is equivalent to assuming that $\mathbf{j}_r \ll \mathbf{j}_\theta$.⁴ Then, by integrating the steady state version of equation (5), we arrive at

$$\left[\lambda(r) \frac{\partial}{\partial r} (r B_\phi) \right]_r^R \approx - \sin \theta \int_r^R dr' r'^2 \left(\frac{\partial \Omega}{\partial r'} B_r + \frac{1}{r'} \frac{\partial \Omega}{\partial \theta} B_\theta \right) . \quad (6)$$

With axial symmetry,

$$j_\theta = - \frac{1}{\mu_0 r} \frac{\partial}{\partial r} (r B_\phi) , \quad (7)$$

so

$$j_\theta(r, \theta) = \frac{-\sin \theta}{\mu_0 r \lambda(r)} \int_r^R dr' r'^2 \left(\frac{\partial \Omega}{\partial r'} B_r + \frac{1}{r'} \frac{\partial \Omega}{\partial \theta} B_\theta \right) + \frac{R \lambda(R)}{r \lambda(r)} j_\theta(R, \theta) . \quad (8)$$

Thus $j_\theta(r, \theta)$ is determined up to an unknown function of θ , namely $j_\theta(R, \theta)$, the current density in the ionosphere.⁵ There is a simpler and more intuitive way to derive equation (8). Start from $\nabla \times \mathbf{E} = 0$ and $\mathbf{F} = \mathbf{E} + \mathbf{U} \times \mathbf{B}$. Express the former in terms of a line integral around a circuit consisting of two small arcs of the same angular width $\delta\theta$, one at r and the other at R , connected

⁴A toy problem illustrating the effects that $H_\lambda \ll H_\rho$ has on \mathbf{j} is presented in the Appendix.

⁵ $\lambda(r)$ is extremely large, effectively infinite, in the neutral atmosphere but decreases dramatically in the ionosphere.

by radial segments of length $\delta r = R - r$. Eliminate the components of \mathbf{E} in terms of those of \mathbf{F} and $\mathbf{U} \times \mathbf{B}$. Then use $\mathbf{j} = \sigma \mathbf{F}$ to replace the components of \mathbf{F} in terms of those of \mathbf{j} . Make the assumption $|j_r| \ll |j_\theta|$ and equation (8) is derived.

Next, we estimate the size of the rhs of equation (8). Let T_1 and T_2 denote the first and second terms, respectively. Steady state, axisymmetric currents cannot close within the ionosphere. Nor can they penetrate inside the planet due to the extremely low conductivity of its neutral atmosphere. However, they can and do flow along field lines into the magnetosphere. These currents produce torques which transfer angular momentum from the planet's spin to plasma that is drifting outward in the magnetosphere. In so doing, they tend to maintain that plasma in approximate corotation with the planet. The torque, and hence $j_\theta(R, \theta)$, are proportional to $\Omega \dot{M}$, where \dot{M} is the rate at which plasma is expelled from the magnetosphere. Because the zonal winds cause Ω to vary by only a few percent, $j_\theta(R, \theta)$ is a weak function of θ . Thus, to a first approximation, T_1 and T_2 are uncorrelated, so the magnitude of $j_\theta(r, \theta)$ is that of the larger of these terms. We take a conservative approach and accept the well-determined value of the first term as the minimum value for $|j_\theta(r, \theta)|$. This is equivalent to treating the ionosphere as an equipotential surface in the reference frame rotating with planet's mean angular velocity.

Ohmic dissipation per unit volume is equal to the square of the current density divided by the electric conductivity. Since j_θ is dominant, we apply equation (8) to obtain the total Ohmic dissipation above radius r ;

$$P \approx \frac{2\pi}{\mu_0} \int_r^R \frac{dr'}{\lambda(r')} \int_0^\pi d\theta \sin^3 \theta \left[\int_{r'}^R dr'' r''^2 \left(\frac{\partial \Omega}{\partial r''} B_r + \frac{1}{r''} \frac{\partial \Omega}{\partial \theta} B_\theta \right) \right]^2. \quad (9)$$

For Ω constant on cylinders, the term in round brackets reduces to $(\partial \Omega / \partial \varpi'') B_\varpi$, where $\varpi = r \sin \theta$. Thus Ohmic dissipation vanishes both for solid body rotation and for a poloidal field aligned parallel to the rotation axis.

b. Estimation of Ohmic dissipation inside Jupiter and Saturn.

We apply equation (9) to evaluate the total Ohmic dissipation above radius r . Atmospheric zonal flows observed on Jupiter and Saturn (Porco et al. 2003, 2005) are taken to be constant on cylinders outside a spherical truncation radius and to vanish inside. Since the observed zonal flows are not exactly N-S symmetric, we construct N-S symmetric profiles by reflecting the northern hemisphere zonal flow about the equator.⁶ The magnetic fields of Jupiter and Saturn have been measured by various spacecrafts and fit by models dominated by a dipole plus smaller quadrupole and octupole components (Connerney 1993). We adopt the axisymmetric part of these field models in our calculations.

Total Ohmic dissipation is plotted against truncation radius in Figure (3) for Jupiter and Saturn. It matches the planet's net luminosity at radii of $0.96 R_J$ and $0.86 R_S$. The magnetic diffusivity at the radius of maximum penetration is $10^7 \text{ m}^2 \text{ s}^{-1}$ for Jupiter and $3 \times 10^6 \text{ m}^2 \text{ s}^{-1}$ for Saturn. By comparison, the magnetic diffusivity is at about $4 \text{ m}^2 \text{ s}^{-1}$ at the planet's outer metallic cores located at $0.84 R_J$ and $0.63 R_S$, respectively.

The magnitudes of the induced toroidal magnetic field and the associated poloidal current are each inversely proportional to λ and thus increase inward. In figure (4) we display the toroidal magnetic field as a function of co-latitude at the maximum penetration depth. It reaches a magnitude of about 15.0 G for Jupiter and about 0.5 G for Saturn.

The above estimates are based on the downward continuation of the observed poloidal magnetic field. This is a reasonable procedure provided the magnetic Reynolds number based on the convective velocity is much smaller than unity above the radius of maximum penetration.

⁶We have verified that using the reflected southern hemisphere zonal flow makes a negligible difference to our results.

4. Ohmic Dissipation For Poloidal Field Lines Aligned With The Rotation Axis

Magnetic fields produced in some dynamo simulations show significant alignment of poloidal field lines parallel to the rotation axis (Glatzmaier 2005). Such alignment would reduce Ohmic dissipation associated with differential rotation since this dissipation is proportional to $(d\Omega/d\varpi)B_\varpi$. However, alignment can only occur in regions where $R_m^c \gtrsim 1$, so its overall effect on the maximum penetration depth of atmospheric zonal winds on Jupiter and Saturn is not obvious.

To examine the effects of alignment on Ohmic dissipation, we consider a model in which the magnetic field is perfectly aligned inside a sphere of radius $r_* < R$ (See figure 5),

$$B_\varpi = 0 \quad \text{and} \quad B_z = B_0 \left[1 - (\varpi/r_*)^2 \right]^{(p-1)}, \quad (10)$$

with p a positive integer. The constant B_0 is set to match the planet's external magnetic dipole. For larger p , the internal magnetic field is more concentrated towards the rotation axis.

The spherical shell $r = r_*$ marks the outer boundary of the dynamo region. For $r < r_*$, $R_m^c > 1$ and the poloidal components of the fluid motions and magnetic field are strongly coupled. We assume that the dynamo maintains the aligned poloidal magnetic field against Ohmic decay. For $r > r_*$, the poloidal magnetic field is taken to be a potential field. Differential rotation acting on the poloidal magnetic field produces a toroidal magnetic field as described in §3.

Outside r_* , $\nabla \times \mathbf{B} = 0$,

$$\begin{aligned} B_r &= \sum_{n=1}^{\infty} 2n (R/r)^{2n+1} P_{2n-1}^0(\cos\theta) g_{2n-1} \\ B_\theta &= - \sum_{n=1}^{\infty} (R/r)^{2n+1} P_{2n-1}^1(\cos\theta) g_{2n-1}. \end{aligned} \quad (11)$$

In order to match the internal field with the external field, we expand the internal field into spherical harmonics at r_* ,

$$\begin{aligned} B_r &= B_0 \sum_{n=1}^{\infty} v_{2n-1} P_{2n-1}^0(\cos\theta) \\ B_\theta &= B_0 \sum_{n=1}^{\infty} w_{2n-1} P_{2n-1}^1(\cos\theta), \end{aligned} \quad (12)$$

with

$$\begin{aligned} v_{2n-1} &= \frac{(4n-1)}{2} \int_{-1}^1 dx x^{2p-1} P_{2n-1}^0(x) \\ w_{2n-1} &= -\frac{(4n-1)}{4(2n-1)n} \int_{-1}^1 dx x^{2p-1} (1-x^2)^{1/2} P_{2n-1}^1(x). \end{aligned} \quad (13)$$

The radial component of the magnetic field is continuous across r_* . Thus

$$g_{2n-1} = (r_*/R)^{2n+1} v_{2n-1} B_0 / (2n), \quad (14)$$

where $B_0 = 2(R/r_*)^3 g_1 / v_1$ in order that g_1 match the planet's external dipole moment.

Ohmic dissipation comes from three sources: the surface current at r_* , the current associated with the nonuniform field inside r_* (for $p > 1$), and the current which arises from interaction of the vacuum field with the zonal flow outside r_* . We treat each of these in turn.

a. Dissipation due to surface current

Because B_θ is discontinuous across r_* , the associated surface current, $J_s = \Delta B_\theta / \mu_0$, would give rise to infinite Ohmic dissipation. However, the transition between internal and external field should be spread across a length scale of order the scale height of the magnetic diffusivity, H_λ .

Then Ohmic dissipation from the surface current evaluates to

$$P \approx \frac{2\pi r_*^2 \lambda}{H_\lambda \mu_0} \int_{-1}^1 dx (\Delta B_\theta(x))^2 = \frac{8n(2n-1)\pi r_*^2 \lambda B_0^2}{(4n-1)\mu_0 H_\lambda} \sum_{n=1}^{\infty} \left(\frac{v_{2n-1}}{2n} + w_{2n-1} \right)^2. \quad (15)$$

Plots of Ohmic dissipation due to the surface current as a function of r_* for different values of p are displayed in figure (6).

*b. Dissipation due to current inside r_**

The azimuthal current density

$$\mathbf{j}_\phi = -\frac{1}{\mu_0} \frac{\partial B_z}{\partial \varpi} = \frac{2(p-1)B_0}{\mu_0} \left(\frac{\varpi}{r_*^2} \right) \left(1 - \frac{\varpi^2}{r_*^2} \right)^{p-2} \quad (16)$$

produces Ohmic dissipation in a layer of thickness H_λ given by

$$P \approx \frac{2\pi r_*^2 \lambda H_\lambda}{\mu_0} \int_0^\pi \left(\frac{\partial B_z}{\partial \varpi} \right)^2 \sin \theta d\theta = \frac{32\pi(p-1)^2 \lambda H_\lambda B_0^2}{(4p-5)(4p-7)\mu_0}. \quad (17)$$

Figure (7) displays the internal dissipation as a function of r_* for different values p .

c. *Ohmic dissipation due to action of the zonal wind on the poloidal magnetic field.*

$B_\varpi \neq 0$ for $r > r_*$, so Ohmic dissipation results from the action of the zonal wind on the poloidal magnetic field. We evaluate it with the aid of equation (9) and plot the results in figure (8).

d. *Total Ohmic dissipation*

The total Ohmic dissipation from all three sources is plotted as a function of r_* in figure (9) for different values of p . Comparison with figure (3) reveals that alignment does not significantly increase the maximum penetration depth of zonal winds on Jupiter and Saturn beyond that calculated in §3 by downward extrapolation of their external magnetic fields.

The arguments in this section do not refer to the magnetic Reynolds number, R_m^c , associated with the convective velocity. Thus the maximum penetration depth we deduce is independent of this quantity. Nevertheless, in reality, the model field we investigate only makes physical sense if $R_m^c \gg 1$ at r_* .

5. How Deep Do The Zonal Flows Penetrate?

Together, §3 and §4 place an upper limit on the depth to which the zonal winds observed in the atmosphere of a giant planet could penetrate. Here we address the more difficult issue of how deeply they actually do penetrate. In particular, do they extend unabated into the convective envelope. It proves convenient to work in cylindrical coordinates (ϖ, ϕ, z) .

The Navier-Stokes equation which governs the motion of the fluid reads

$$\frac{\partial \mathbf{U}}{\partial t} + (\mathbf{U} \cdot \nabla) \mathbf{U} + 2\Omega_P \times \mathbf{U} = -\frac{\nabla p}{\rho} - \nabla \Phi_{\text{tot}} + \frac{(\nabla \times \mathbf{B}) \times \mathbf{B}}{\mu_0 \rho}, \quad (18)$$

where \mathbf{U} is the total velocity measured relative to a frame rotating at angular speed Ω_P (the assumed uniform angular velocity of the planet's metallic core), ρ is the density, p is the pressure, and Φ_{tot} is the gravitational plus centrifugal potential.⁷ We express the steady-state limit of this

⁷We ignore the utterly negligible viscous stress.

equation as

$$2\Omega_P \times \bar{\mathbf{U}} = -\frac{\nabla \bar{p}}{\bar{\rho}} - \nabla \bar{\Phi}_{\text{tot}} + \bar{\mathbf{a}}, \quad (19)$$

where the overbar denotes time average and

$$\bar{\mathbf{a}} = \frac{(\nabla \times \mathbf{B}) \times \mathbf{B}}{\mu_0 \bar{\rho}} - \frac{(\mathbf{U} \cdot \nabla) \mathbf{U}}{\mu_0 \bar{\rho}}, \quad (20)$$

Smaller terms that involve fluctuations of ρ , p , and Φ_{tot} have been discarded. Individually, the first and second terms on the rhs of equation (19) are larger, by far, than the others. Thus

$$\frac{\nabla \bar{p}}{\bar{\rho}} \approx -\nabla \bar{\Phi}_{\text{tot}}. \quad (21)$$

Taking the curl of equation (19), we arrive at

$$2\Omega_P \frac{\partial \bar{U}_\phi}{\partial z} = - \frac{\partial \ln \rho}{\partial s} \bigg|_p (\nabla \bar{s} \times \bar{\mathbf{g}}) \cdot \mathbf{e}_\phi - (\nabla \times \bar{\mathbf{a}}) \cdot \mathbf{e}_\phi, \quad (22)$$

with $\bar{\mathbf{g}} = -\nabla \bar{\Phi}_{\text{tot}}$. Thus $\partial \bar{U}_\phi / \partial z = 0$ for an uniform composition isentrope in the absence of Reynolds and Maxwell stresses. This is the Taylor-Proudman state. Next we bound departures from this state that each term on the rhs of equation (22) could produce.

a. Buoyancy

1). IN THE CONVECTIVE ENVELOPE

Here we are entering uncertain territory. Convection transports the net luminosity in the fluid interior, but our understanding of turbulent convection is limited even for nonrotating systems. Rotation and especially strong differential rotation add additional complexity. It is not obvious which of the terms on the rhs of equation (22) is dominant for conditions appropriate to a convective envelope.

We are guided by Ingersoll & Pollard (1982) who model convection under conditions of strong differential rotation which shears convective cell in the azimuthal direction. They argue that under these conditions, the magnitude of the component of $\nabla \bar{s}$ along $\bar{\mathbf{g}}$ must satisfy

$$g \left| \frac{\partial \ln \rho}{\partial s} \right|_p \frac{|\nabla \bar{s} \cdot \bar{\mathbf{g}}|}{|\bar{\mathbf{g}}|} \sim \left(\frac{\partial U_\phi}{\partial \varpi} \right)^2; \quad (23)$$

In other words, the Richardson number based on the rate of shear is of order unity.

The variation of \bar{U}_ϕ along z depends upon the component of ∇s that is orthogonal to both \bar{g} and \mathbf{e}_ϕ about which mixing length models are silent. We parameterize this component in terms of $\nabla s \cdot \hat{\bar{g}}$ and the angle δ between ∇s and \bar{g} . Buoyancy drives convection, so it is to be expected that $\delta \ll 1$. Combining equations (22) and (23) yields

$$\left| \frac{H_\rho}{U_\phi} \frac{\partial U_\phi}{\partial z} \right| \sim \frac{H_\rho}{2\Omega_P U_\phi} \left(\frac{\partial U_\phi}{\partial \varpi} \right)^2 \tan \delta. \quad (24)$$

Since \bar{g} is approximately aligned along the *spherical* radial direction, $|\nabla s| \tan \delta$ is essentially the magnitude of latitudinal component of ∇s .

At the maximum penetration depth,

$$\left| \frac{H_\rho}{\bar{U}_\phi} \frac{\partial \bar{U}_\phi}{\partial z} \right| \sim 0.6 \tan \delta \quad (25)$$

for Jupiter, and

$$\left| \frac{H_\rho}{\bar{U}_\phi} \frac{\partial \bar{U}_\phi}{\partial z} \right| \sim 0.3 \tan \delta. \quad (26)$$

for Saturn. As stated above, we expect that $\tan \delta \ll 1$. Moreover, its numerical coefficients is proportional to H_ρ , which decreases outward. Thus buoyancy is unlikely to effect a significant departure from the Taylor-Proudman state in the convective envelope.

2). IN THE RADIATIVE ATMOSPHERE

There are conflicting views about the strength of the static stability in the radiative atmospheres of Jupiter and Saturn and the depth to which stable layers extend. Here we consider how Taylor-Proudman columns might be truncated in strongly stable layers in which s changes on the same *spherical* radial scale as ρ . In such layers

$$\left| \frac{\partial \ln \rho}{\partial s} \right|_p H_\rho |\nabla s| \sim 1 \quad (27)$$

in equation (22) to obtain

$$\left| \frac{H_\rho}{\bar{U}_\phi} \frac{\partial \bar{U}_\phi}{\partial z} \right| \sim \frac{g}{2\Omega_P \bar{U}_\phi} \tan \delta. \quad (28)$$

Numerical evaluation yields

$$\left| \frac{H_\rho}{\bar{U}_\phi} \frac{\partial U_\phi}{\partial z} \right| \sim 600 \tan \delta. \quad (29)$$

for Jupiter, and

$$\left| \frac{H_\rho}{\bar{U}_\phi} \frac{\partial \bar{U}_\phi}{\partial z} \right| \sim 200 \tan \delta. \quad (30)$$

for Saturn. Taylor-Proudman columns could be truncated in the radiative atmosphere provided surfaces of constant entropy were inclined to those of constant potential in the latitudinal direction by more than a fraction of a degree. The resulting velocity field would constitute a strong thermal wind.

b. Magnetic stresses

Deviations from the Taylor-Proudman state caused by Maxwell stresses follow from

$$\left| \frac{H_\rho}{\bar{U}_\phi} \frac{\partial \bar{U}_\phi}{\partial z} \right| = \frac{H_\rho}{2\mu_0 \Omega_P |\bar{U}_\phi|} \left| \mathbf{e}_\phi \cdot \nabla \times \left(\frac{(\nabla \times \mathbf{B}) \times \mathbf{B}}{\bar{\rho}} \right) \right| \sim \frac{H_\rho \bar{B}^2}{2\mu_0 \Omega_P |\bar{U}_\phi| \bar{\rho} \ell^2}, \quad (31)$$

where ℓ is the typical scale over which \mathbf{B} varies. The order of magnitude estimate assumes $\ell \lesssim H_\rho$.

Next we bound \bar{B}^2/ℓ^2 by applying the Ohmic constraint. The latter reduces to

$$\frac{4\pi\lambda R^2 H_\rho \bar{B}^2}{\mu_0 \ell^2} \lesssim \mathcal{L}. \quad (32)$$

Eliminating \bar{B}^2/ℓ^2 between equations (31) and (32), we arrive at

$$\left| \frac{H_\rho}{\bar{U}_\phi} \frac{\partial \bar{U}_\phi}{\partial z} \right| \lesssim \frac{\mathcal{L}}{8\pi\lambda\Omega_P |\bar{U}_\phi| \rho R^2}. \quad (33)$$

Numerical evaluation yields

$$\left| \frac{H_\rho}{\bar{U}_\phi} \frac{\partial \bar{U}_\phi}{\partial z} \right| \lesssim 10^{-5} \quad (34)$$

at the maximum penetration depths in Jupiter and Saturn. Moreover, this ratio decreases sharply outward. Clearly, magnetic stresses are incapable of truncating the observed zonal flows.

c. Reynolds stresses

Departures from the Taylor-Proudman state caused by Reynolds stresses obey

$$\left| \frac{H_\rho}{\bar{U}_\phi} \frac{\partial \bar{U}_\phi}{\partial z} \right| = \frac{H_\rho}{2\Omega_P |\bar{U}_\phi|} \left| \mathbf{e}_\phi \cdot \nabla \times \left(\bar{U} \cdot \nabla \right) \bar{U} \right|. \quad (35)$$

We treat separately contributions from the mean axisymmetric flow, $\bar{\mathbf{U}}$, and from fluctuations about it, $\mathbf{u} = \mathbf{U} - \bar{\mathbf{U}}$.

The sole contribution involving \bar{U}_ϕ can be absorbed by adding \bar{U}_ϕ/ϖ to Ω_P on the lhs of equation (19) and in what follows. We do not consider it further. The poloidal part of $\bar{\mathbf{U}}$, denoted by $\bar{\mathbf{U}}_p$, describes meridional circulation. It yields

$$\left| \frac{H_\rho}{\bar{U}_\phi} \frac{\partial \bar{U}_\phi}{\partial z} \right| \sim \frac{\bar{U}_p^2}{2\Omega_P |\bar{U}_\phi| H_\rho}, \quad (36)$$

where the variation scale of \bar{U}_p is set to H_ρ . With parameters appropriate to Jupiter and Saturn, the rhs of equation (36) is $\ll 1$ for $|\bar{U}_p| \ll |\bar{U}_\phi|$.

Velocity fluctuations contribute

$$\left| \frac{H_\rho}{\bar{U}_\phi} \frac{\partial \bar{U}_\phi}{\partial z} \right| \sim \frac{H_\rho \bar{u}_\phi^2}{2\Omega_P |\bar{U}_\phi| \ell_p \ell_\phi}, \quad (37)$$

where ℓ_p and ℓ_ϕ are the meridional and azimuthal scales of the convective cells. In deriving equation (37), we note that azimuthal stretching of eddies by strong differential rotation results in $\ell_\phi \gtrsim \ell_p$ and mass conservation implies $u_p \ell_\phi \sim u_\phi \ell_p$. To bound \bar{u}_ϕ^2 , we follow Ingersoll & Pollard (1982) and adopt $|\partial \bar{U}_\phi / \partial \varpi| (\ell_p / \ell_\phi)$ as the convective rate. In each scale height, turbulent mechanical energy is dissipated as heat at a rate $\sim \mathcal{L}$. Hence

$$4\pi R^2 H_\rho \bar{\rho} \bar{u}_\phi^2 \frac{\partial \bar{U}_\phi}{\partial \varpi} \frac{\ell_p}{\ell_\phi} \sim \mathcal{L}. \quad (38)$$

Together, equations (37) and (38) yield

$$\left| \frac{H_\rho}{\bar{U}_\phi} \frac{\partial \bar{U}_\phi}{\partial z} \right| \sim \frac{\mathcal{L}}{8\pi\Omega_P |\bar{U}_\phi| |\partial \bar{U}_\phi / \partial \varpi| \bar{\rho} R^2 \ell_p^2} \lesssim \frac{\mathcal{L}}{8\pi\Omega_P \bar{U}_\phi^2 \bar{\rho} R^3 \Delta\theta}, \quad (39)$$

where $\Delta\theta$ denotes the typical latitudinal width of the zonal jets. In accord with Ingersoll & Pollard (1982), we set $|\partial \bar{U}_\phi / \partial \varpi| \sim |\bar{U}_\phi| / \ell_p$ in arriving at the final form of equation (39). Numerical

evaluation with parameters appropriate to the tops of the convection zones in Jupiter and Saturn gives

$$\left| \frac{H_\rho}{\overline{U}_\phi} \frac{\partial \overline{U}_\phi}{\partial z} \right| \lesssim 10^{-5}. \quad (40)$$

d. Maximum width of an equatorial jet

A sufficiently narrow equatorial jet could maintain constant velocity on cylinders throughout the planet. As an example, we consider the specific velocity profile

$$\overline{U}_\phi = U_{\phi 0} \sin \left(\frac{\pi}{2} \frac{(\theta - \theta_0)}{(\pi/2 - \theta_0)} \right)^{\frac{1}{10}} \quad \text{if } \theta < \pi - \theta_0; \quad (41)$$

and,

$$\overline{U}_\phi = 0 \quad \text{if } \theta < \theta_0 \text{ and } \theta > \pi - \theta_0; \quad (42)$$

so the jet has equatorial velocity $U_{\phi 0}$ and angular half-width $\pi/2 - \theta_0$. For Jupiter and Saturn, $U_{\phi 0}$ is approximately 140 m s^{-1} and 400 m s^{-1} , respectively. Figure (10) displays the calculated Ohmic dissipation rate as a function of the jet half-width. The maximum half-width is about 18.5° for Jupiter, and 35.5° for Saturn. The maximum half widths are related to the fractional radii of maximum penetration, r_{mp}/R , calculated in section 3 by

$$\cos \theta_0 \approx \frac{r_{mp}}{R}. \quad (43)$$

6. Discussion.

The condition that the total Ohmic dissipation not exceed the planet's net luminosity sets an upper bound on the depth to which the zonal flows observed in the atmospheres of Jupiter and Saturn could penetrate. At these depths, the magnetic Reynolds number, based on the observed zonal winds and the scale height of the magnetic diffusivity, is of order unity.

We consider it unlikely that the observed flows extend to the depth of maximum penetration because that would require the Taylor-Proudman constraint to be violated in the convective envelope. We have been unable to identify any plausible mechanism that could do this. Lack of a

rigorous model for convection is a weakness. We base our analysis of the robustness of the Taylor-Proudman constraint on the mixing length model designed by Ingersoll & Pollard (1982) to apply under conditions of strong differential rotation. However, we have confirmed that the conclusions we draw from it also follow from other convection models that consider only solid body rotation, or even those that neglect the effects of rotation entirely.

The boundaries of the cylindrical extensions of the equatorial jets essentially coincide with the maximum penetration depths. Thus these jets could maintain constant velocities along cylinders through the planets. Winds measured at $7.4^\circ N$ by the Galileo probe as it descended into Jupiter are consistent with this possibility.

Acknowledgments We are grateful for support from the NASA Planetary Geology and Geophysics program.

7. Appendix

We calculate the current distribution arising from a vacuum axial dipole field and a simple zonal flow. The angular velocity, Ω , is taken to be of the form

$$\Omega = \Omega_P + \frac{\Omega_{out}}{1 + \exp [c_{mp}(r_{mp} - r)]}. \quad (44)$$

Here c_{mp} is the truncation factor and r_{mp} is the truncation radius. $\Omega(r) \rightarrow \Omega_P$ for $r < r_{mp}$ and $\Omega(r) \rightarrow \Omega_P + \Omega_{out}$ for $r > r_{mp}$.⁸

The current density arising from interaction of this flow with a vacuum dipole magnetic field satisfies:

$$\nabla \times \frac{\mathbf{j}}{\sigma} = \nabla \times \{[(\Omega - \Omega_P) \mathbf{e}_z \times \mathbf{r}] \times \mathbf{B}\} = -\frac{2M}{3r^2} \frac{d\Omega}{dr} \frac{dP_2}{d\theta} \mathbf{e}_\phi, \quad (45)$$

where M is the dipole moment.

Because $\nabla \cdot \mathbf{j} = 0$, \mathbf{j} can be derived from a vector potential A such that

$$\mathbf{j} = \nabla \times (A \mathbf{e}_\phi), \quad (46)$$

⁸We plot $\Omega - \Omega_P$ as a function of scaled radius in figure (11).

where

$$A = \frac{-rf(r)}{6} \frac{dP_2}{d\theta}. \quad (47)$$

By direct computation

$$\nabla \times \frac{\mathbf{j}}{\sigma} = \frac{1}{6r\sigma} \left[\frac{d^2}{dr^2} (r^2 f) - 6f - \frac{d \ln \sigma}{dr} \frac{d}{dr} (r^2 f) \right] \frac{dP_2}{d\theta} \mathbf{e}_\phi. \quad (48)$$

So

$$\frac{d\Omega}{dr} = \frac{-r}{4\sigma M} \left[\frac{d^2}{dr^2} (r^2 f) - 6f - \frac{d \ln \sigma}{dr} \frac{d}{dr} (r^2 f) \right]. \quad (49)$$

At the planet's surface, the current density along the radial direction goes to zero: $f(r) \rightarrow 0$; Near its center, $j \propto r$: $df(r)/dr - f(r)/r \rightarrow 0$. We solve equation (49) to obtain $f(r)$.

Since,

$$\mathbf{j} \cdot \nabla (Ar \sin \theta) = 0, \quad (50)$$

the current density follows the contour lines of $Ar \sin \theta$ and its magnitude satisfies $|\mathbf{j}| = |\nabla (Ar \sin \theta)| / r \sin \theta$. Figure (12) displays the streamlines of current flow.

*References

Ashcroft, N. W. 1968. Metallic hydrogen - a high temperature superconductor. *Phys. Rev. Lett.* **21**, 1748–1749.

Atkinson, D. H., A. P. Ingersoll and A. Seiff 1997. Deep zonal winds on Jupiter: update of Doppler tracking the Galileo probe from the orbiter. *Nature* **338**, 649–650.

Atkinson, D. H., J. B. Pollack and A. Seiff 1998. The Galileo probe Doppler wind experiment: measurement of the deep zonal wind on Jupiter. *J. Geophys. Res.* **103**, 22911–22928.

Aurnou, J. M., and M. H. Heimpel 2004. Zonal jets in rotating convection with mixed mechanical boundary conditions. *Icarus* **169**, 492–498.

Busse, F. H. 1976. Simple model of convection in the Jovian atmosphere. *Icarus* **29**, 255–260.

Busse, F. H. 1983. A model of mean zonal flows in the major planets. *Geophys. Astrophys. Fluid Dyn.* **23**(2), 153–174.

Busse, F. H. 1994. Convection driven zonal flows and vortices in the major planets. *Chaos* **4**, 123–134.

Connerney, J. E. P. 1993. Magnetic field of the outer planets. *J. Geophys. Res.* **98**, 18659–18679.

Dessler, A. J. 1983. Coordinate systems. *Physics of the Jovian magnetosphere* Cambridge University Press, New York, pp. 498–504

Glatzmaier, G. A. 2005 A saturnian dynamo simulation. *American Geophysical Union Fall Meeting 2005, San Francisco, CA*

Guillot, T. 1999 A comparison of the interiors of Jupiter and Saturn. *Plan. Space Sci.*, **47**, 1183–1200

Guillot, T., D. J. Stevenson, W. B. Hubbard and D. Saumon 2004 The interior of Jupiter. *Jupiter: The Planet, Satellites and Magnetosphere* Cambridge University Press, New York, pp 35–57

Guillot, T. 2005. The interior of giant planets: Models and outstanding questions. *Annu. Rev. Earth Planet. Sci.*, **33**, 493–530

Heimpel, M., J. Aurnou and J. Wicht 2005. Simulation of equatorial and high latitude jets on Jupiter in a deep convection model. *Nature* **438**, 193–196

Holmes, N. C., M. Ross and W. J. Nellis 1995. Temperature measurements and dissociation of shock-compressed liquid deuterium and hydrogen. *Phys. Rev. B* **59**, 15835–15845

Hubbard, W. B. 1968. Thermal structure of Jupiter. *Astrophys. J.* **152(3P1)**, 745–754.

Hubbard, W. B., T. Guillot, and J. I. Lunine 1997. Liquid metallic hydrogen and the structure of brown dwarfs and giant planets. *Phys. Plasmas* **4(5)**, 2011–2015

Ingersoll, A. P. and J. N. Cuzzi 1969. Dynamics of Jupiter's cloud bands. *J. Atmos. Sci.* **26**, 981–985.

Ingersoll, A. P. and D. Pollard 1982. Motion in the interiors and atmosphere of Jupiter and Saturn –scale analysis, anelastic equations, barotropic-stability criterion. *Icarus* **52**, 62–80.

Ingersoll, A. P., R. F. Beebe, B. J. Conrath and G. E. Hunt 1984. Structure and dynamics of Saturn's atmosphere. *Saturn* University of Arizona Press, Tucson, pp 195–238

Ingersoll, A. P. 1990. Atmospheric dynamics of the outer planets. *Science* **248**, 308–315.

Liu, J. J. 2006. Interaction of magnetic field and zonal wind in the out shells of giant planets. *Caltech Thesis* **2006**, 47–52.

Nellis, W. J., A. C. Mitchell, P. C. McCandless, D. J. Erskine and S. T. Weir 1992. Electronic energy gap of molecular hydrogen from electrical conductivity measurements at high shock pressures. *Phys. Rev. Lett.* **68**, 2937–2940

Nellis, W. J., M. Ross and N. C. Holmes 1995. Temperature measurements of shock-compressed liquid hydrogen: implication for the interior of Jupiter *Science* **269**, 1249–1252

Nellis, W. J., S. T. Weir and A. C. Mitchell 1996. Metallization and electrical conductivity of fluid hydrogen in Jupiter. *Science* **273**, 936–938

Nellis, W. J., S. T. Weir and A. C. Mitchell 1999. Minimum metallic conductivity of fluid hydrogen at 140 GPa (1.4 Mbar). *Phys. Rev. B* **59**, 3434–3449

Porco, C. C., et al. 2003 Cassini imaging of Jupiter's atmosphere, satellites and rings. *Science* **299**, 1541–1547

Porco, C. C., et al. 2005 Cassini imaging science: initial results on Saturn's atmosphere. *Science* **307**, 1243–1247

Russel, C. T., Z. J. Yu, K. K. Khurana and M. G. Kivelson 2001. Magnetic field changes in the inner magnetosphere of Jupiter. *Adv. Space Res.* **28**(6), 897–902.

Russel, C. T., Z. J. Yu, K. K. Khurana, S. P. Joy and M. G. Kivelson 2001. Secular variation of the Jovian magnetic field from singular value decomposition analysis *American Astronomical Society, DPS meeting* **33**, 1097.

Smith, B. A. and G. E. Hunt 1976. Motions and morphology of clouds in the atmosphere of Jupiter. *Jupiter* University of Arizona Press, Tucson, pp 564-585

Stevenson D. J. and N. W. Ashcroft 1974. Conductors in fully ionized liquid-metals *Phys. Rev. A* **9**(2), 782–789.

Taylor, G. I. 1923. Experiments on the motion of solid bodies in rotating fluids. *Proc. R. Soc. A* **104**, 213–218.

Vasavada A. R. and A. P. Showman 2005. Jovian atmospheric dynamics: An update after Galileo and Cassini. *Rep. Prog. Phys.* **68**, 1935-1996.

Weir, S. T., A. C. Mitchell and W. J. Nellis 1996. Metallization of fluid molecular hydrogen at 140 Gpa. *Phys. Rev. Lett.* **76**, 1860–1863.

List of Figures

1	Electrical conductivity and magnetic diffusivity distributions inside giant planets: (a) Jupiter; (b) Saturn. Values of conductivity and magnetic diffusivity are plotted in the left and right panels, respectively. Solid lines depict mean value; dashed lines bound the range of uncertainties.	25
2	Scale height of magnetic diffusivity as a function of scaled radius: (a) Jupiter; (b) Saturn.	26
3	Observed zonal flow is taken to penetrate along cylinders until it is truncated at r_{mp} . Solid curves display nominal values for the total Ohmic dissipation, P , as a function of r_{mp}/R . Dashed curves bound its uncertainty. Horizontal solid line marks the planet's net luminosity, \mathcal{L} . At r_{mp} , $P = \mathcal{L}$	27
4	Toroidal magnetic field at the maximum penetration depth as a function of colatitude: (a) Jupiter, (b) Saturn.	28
5	Poloidal magnetic field lines for $p = 5$	29
6	Ohmic dissipation due to surface current as a function of r_*/R . (a) Jupiter; (b) Saturn.	30
7	Ohmic dissipation due to internal current as a function of r_*/R . (a) Jupiter; (b) Saturn.	31
8	Ohmic dissipation due to interaction of B_ϖ with $\partial\Omega/\partial\varpi$ as a function of r_*/R . (a) Jupiter; (b) Saturn.	32
9	Total Ohmic dissipation as a function of r_*/R . (a) Jupiter; (b) Saturn.	33
10	Total Ohmic dissipation rate versus jet's angular half-width. Horizontal solid lines mark the planet's net luminosity. Dashed lines indicate the range of uncertainties. Central value of the maximum half-width is 18.5° for Jupiter and 35.5° for Saturn. .	34
11	Angular velocity corresponding to current streamlines shown in figure (12). Parameters in equation (44) are $r_{mp}/R = 0.9$, $c_{mp} = 50$. Surface value of $\Omega_P + \Omega_{out}$ is scaled to be near unity.	35

12 Current stream lines arising from a toy model. A vacuum dipole field interacts with a simple cylindrical flow consisting of a nearly uniformly rotating core and a more rapidly rotating envelope. See text and figure (11) for details. In the outer envelope, the streamlines are close to lines of constant r . Their spacing is inversely proportional to $jr \sin \theta$. Ohmic dissipation per unit volume, $\propto \sigma U_\phi^2 B_p^2$, is maximal near the dash line which marks to core-envelope boundary. Our model only makes sense in regions where the magnetic Reynolds number based on the convective velocity is small. 36

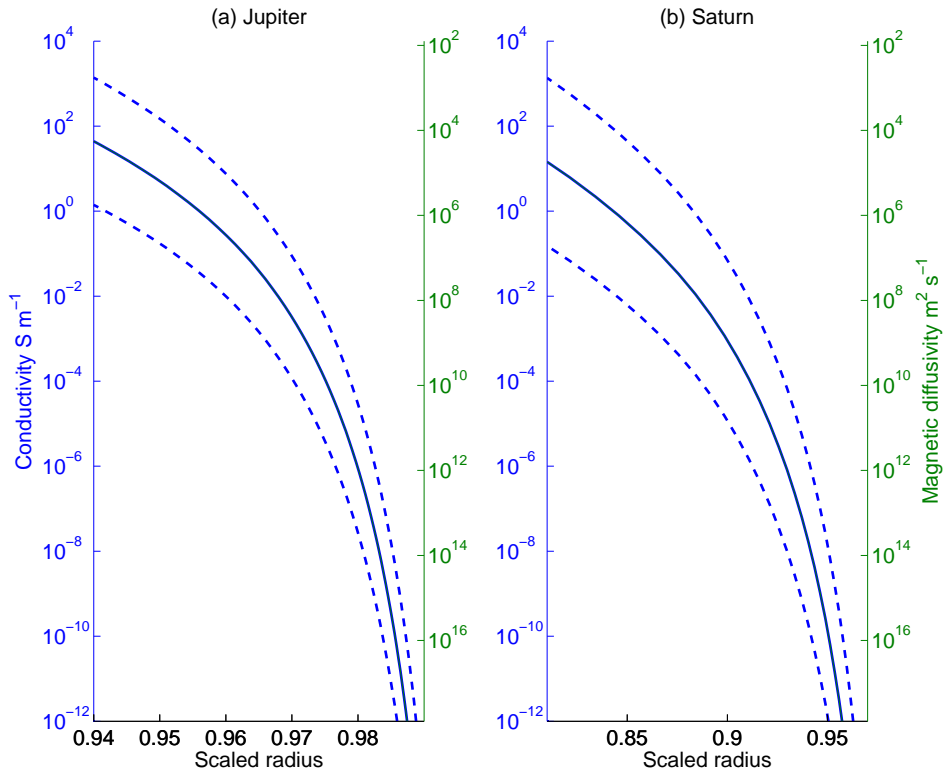


Figure 1: Electrical conductivity and magnetic diffusivity distributions inside giant planets: (a) Jupiter; (b) Saturn. Values of conductivity and magnetic diffusivity are plotted in the left and right panels, respectively. Solid lines depict mean value; dashed lines bound the range of uncertainties.

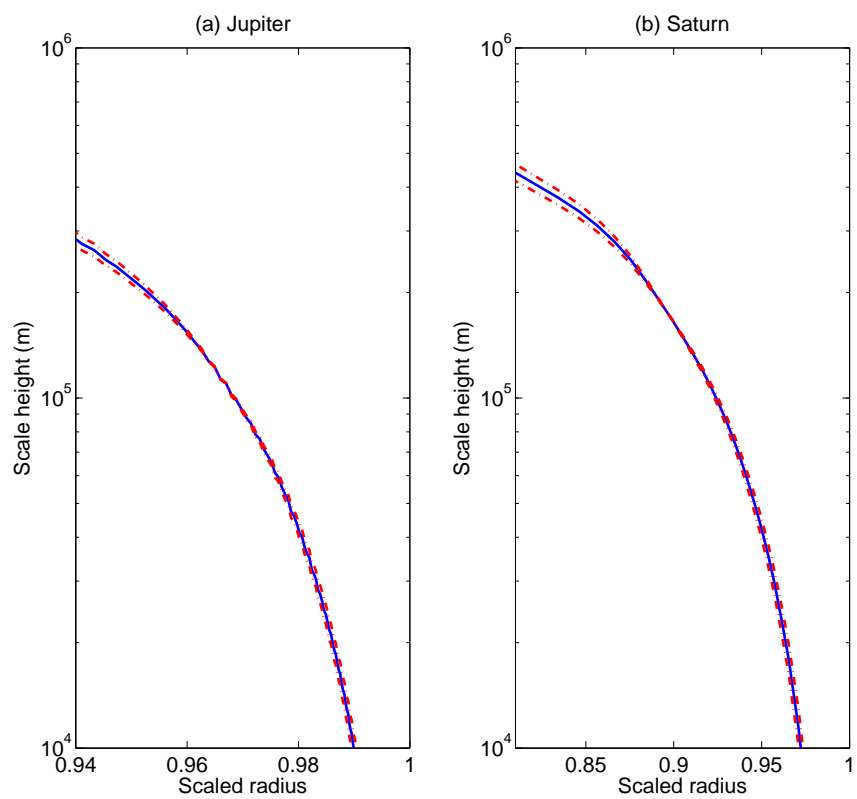


Figure 2: Scale height of magnetic diffusivity as a function of scaled radius: (a) Jupiter; (b) Saturn.

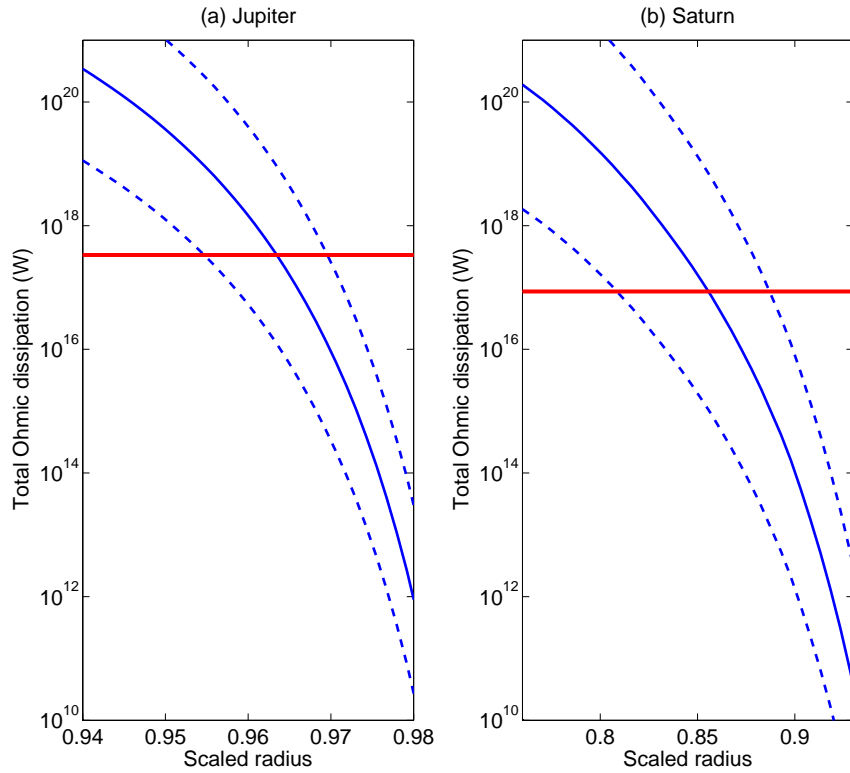


Figure 3: Observed zonal flow is taken to penetrate along cylinders until it is truncated at r_{mp} . Solid curves display nominal values for the total Ohmic dissipation, P , as a function of r_{mp}/R . Dashed curves bound its uncertainty. Horizontal solid line marks the planet's net luminosity, \mathcal{L} . At r_{mp} , $P = \mathcal{L}$.

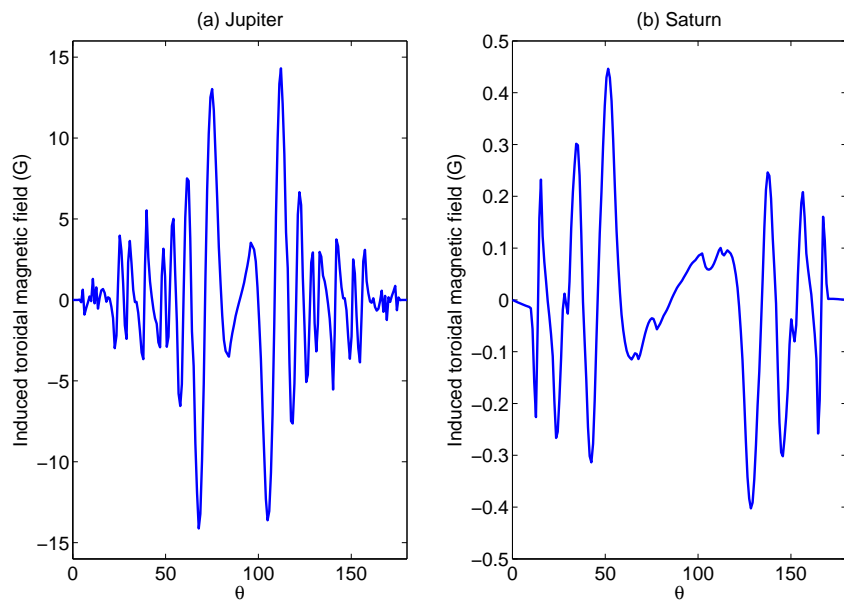


Figure 4: Toroidal magnetic field at the maximum penetration depth as a function of colatitude:
 (a) Jupiter, (b) Saturn.

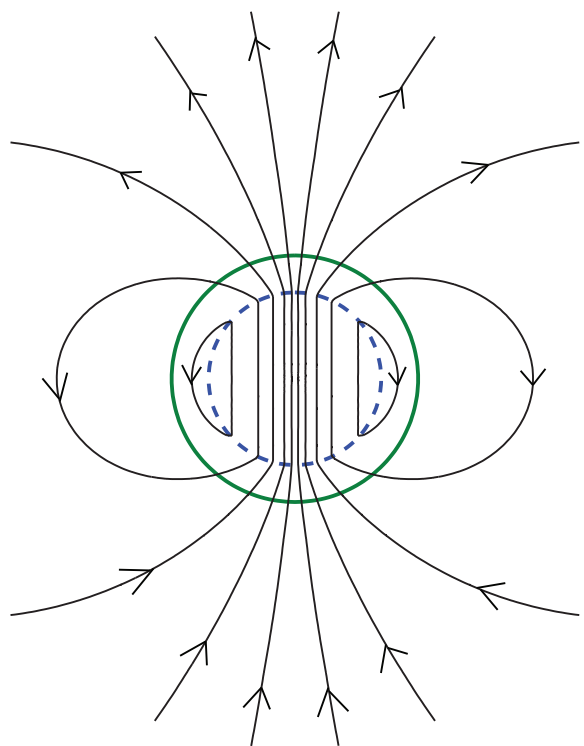


Figure 5: Poloidal magnetic field lines for $p = 5$.

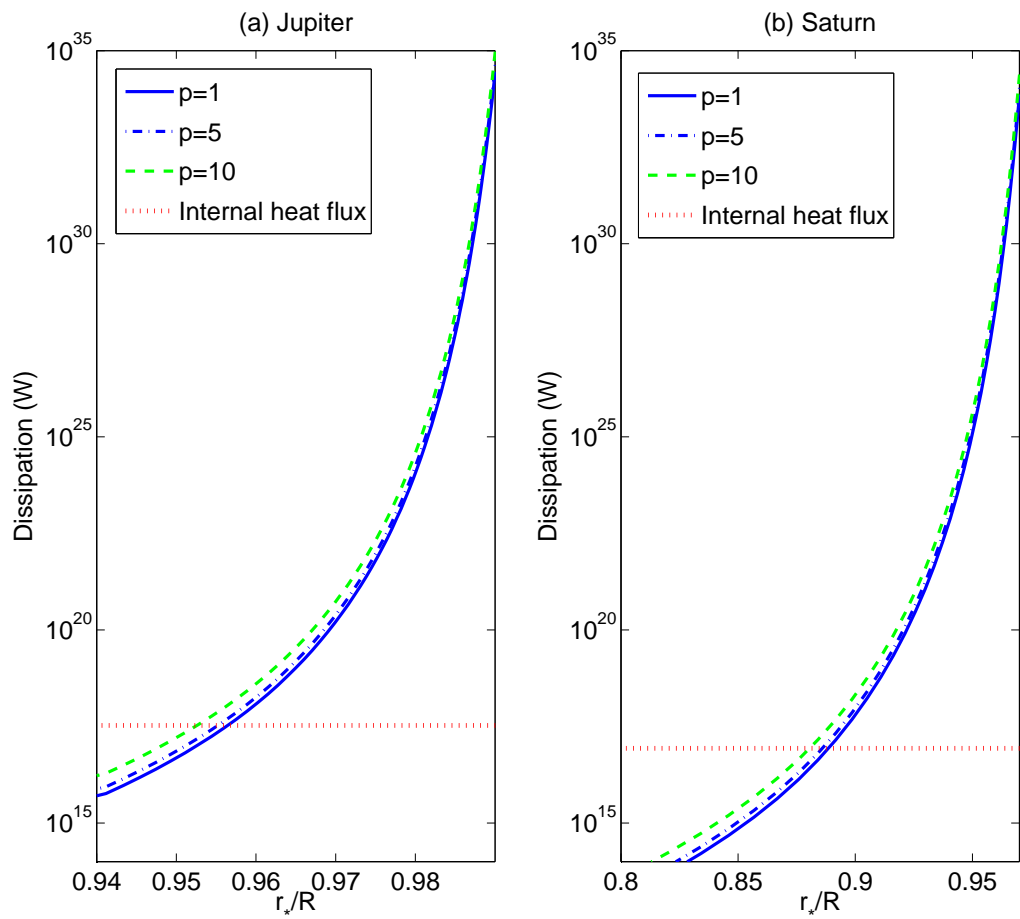


Figure 6: Ohmic dissipation due to surface current as a function of r_*/R . (a) Jupiter; (b) Saturn.

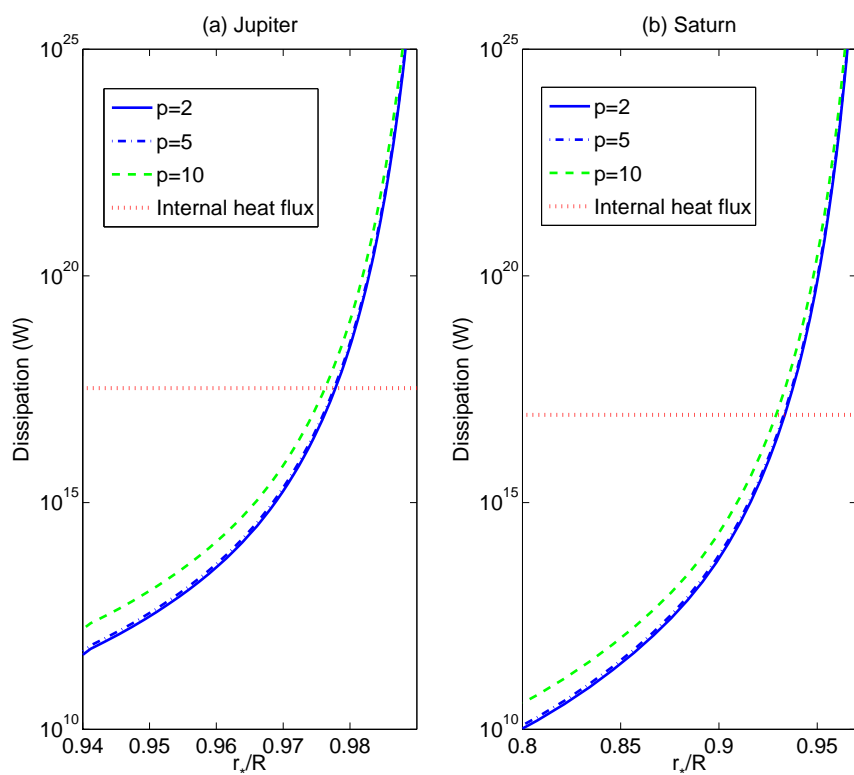


Figure 7: Ohmic dissipation due to internal current as a function of r_*/R . (a) Jupiter; (b) Saturn.

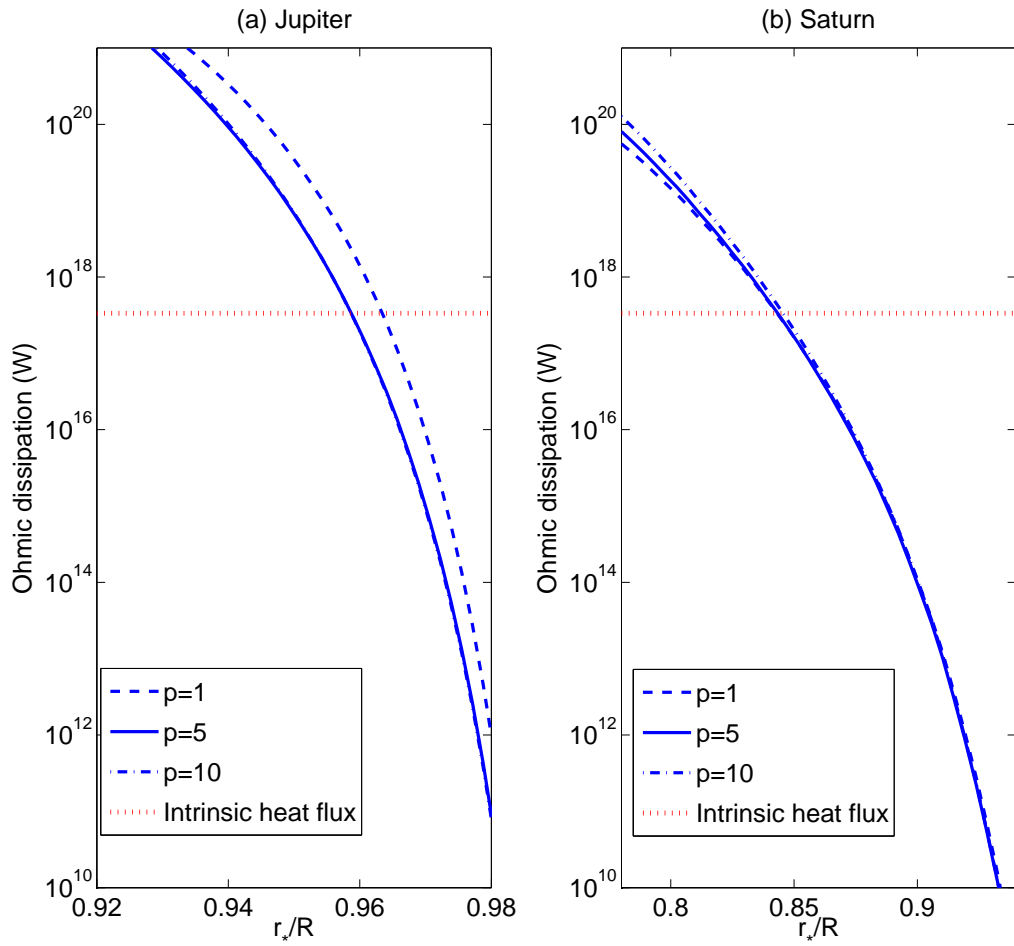


Figure 8: Ohmic dissipation due to interaction of B_ϖ with $\partial\Omega/\partial\varpi$ as a function of r_*/R . (a) Jupiter; (b) Saturn.

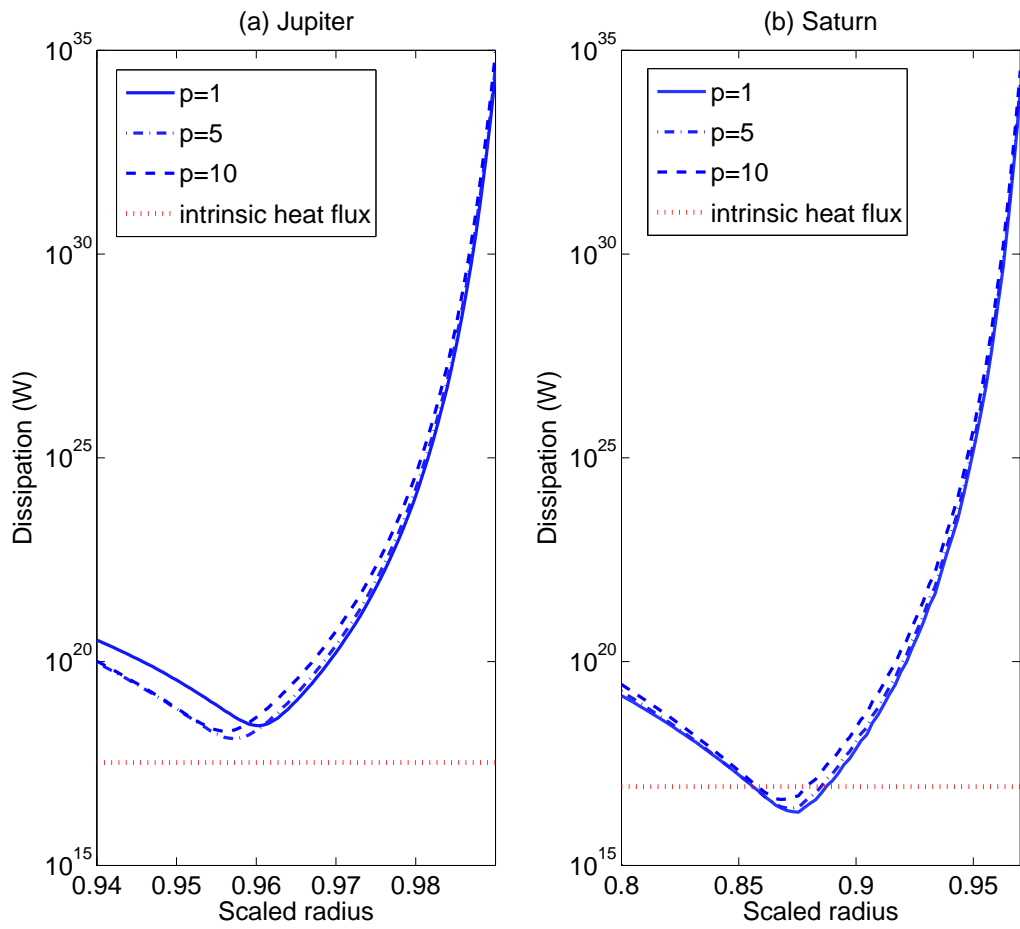


Figure 9: Total Ohmic dissipation as a function of r_*/R . (a) Jupiter; (b) Saturn.

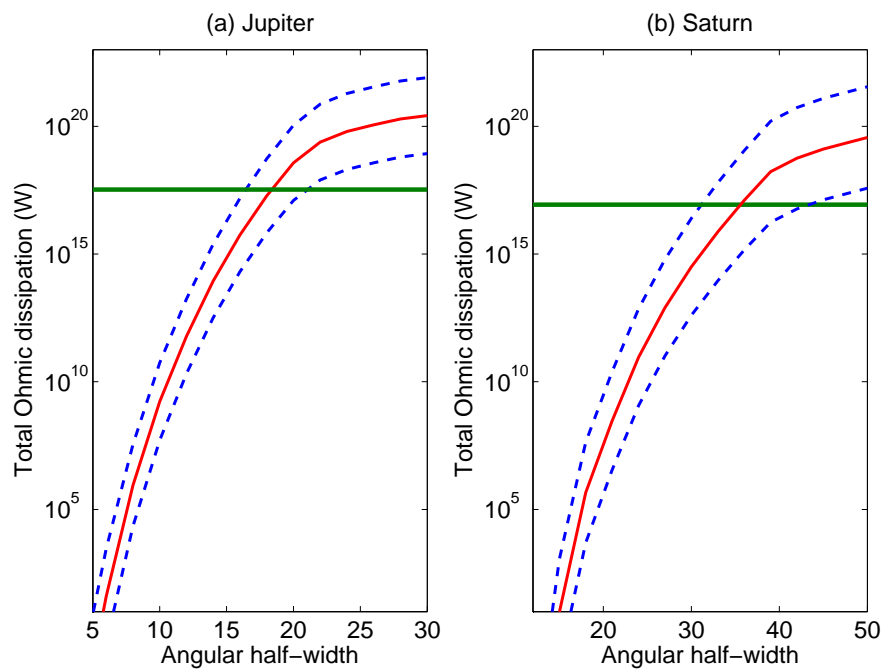


Figure 10: Total Ohmic dissipation rate versus jet's angular half-width. Horizontal solid lines mark the planet's net luminosity. Dashed lines indicate the range of uncertainties. Central value of the maximum half-width is 18.5° for Jupiter and 35.5° for Saturn.

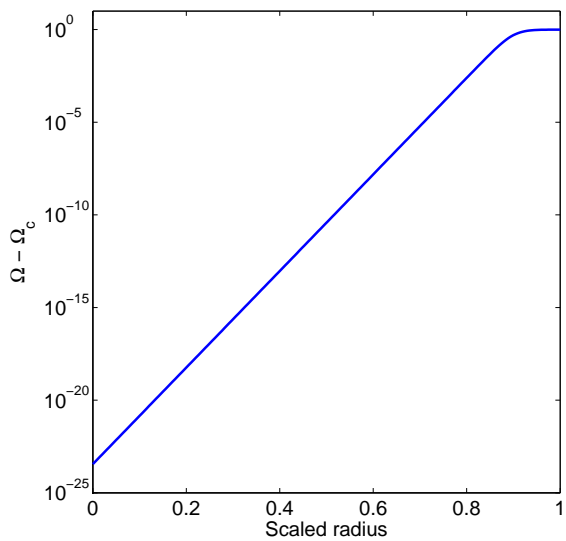


Figure 11: Angular velocity corresponding to current streamlines shown in figure (12). Parameters in equation (44) are $r_{mp}/R = 0.9$, $c_{mp} = 50$. Surface value of $\Omega_P + \Omega_{out}$ is scaled to be near unity.

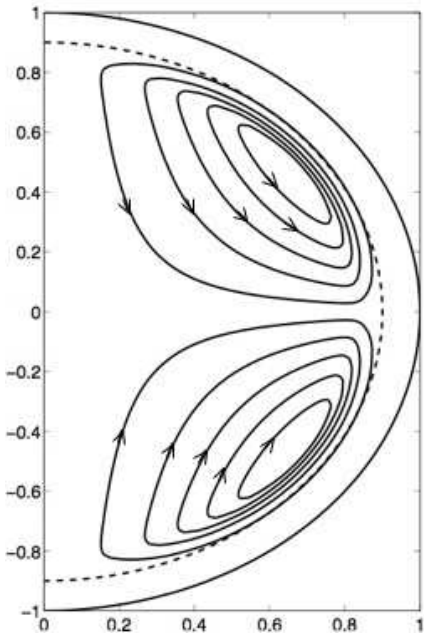


Figure 12: Current stream lines arising from a toy model. A vacuum dipole field interacts with a simple cylindrical flow consisting of a nearly uniformly rotating core and a more rapidly rotating envelope. See text and figure (11) for details. In the outer envelope, the streamlines are close to lines of constant r . Their spacing is inversely proportional to $jr \sin \theta$. Ohmic dissipation per unit volume, $\propto \sigma U_\phi^2 B_p^2$, is maximal near the dash line which marks the core-envelope boundary. Our model only makes sense in regions where the magnetic Reynolds number based on the convective velocity is small.